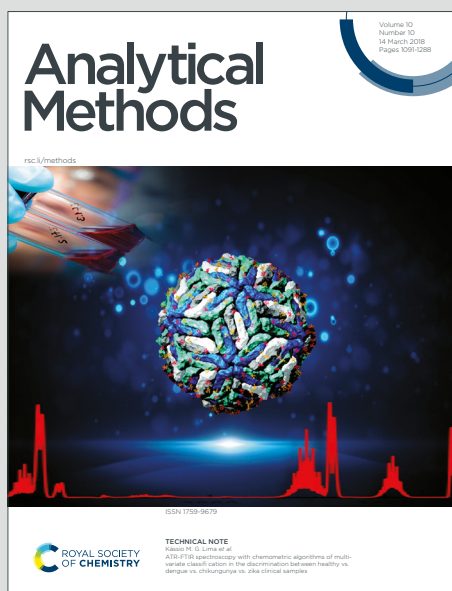


Analytical Methods

Accepted Manuscript

This article can be cited before page numbers have been issued, to do this please use: H. Zhang, N. Rafat, J. Rudge, S. P. Peddireddy, Y. N. Kim, T. Khan and A. Sarkar, *Anal. Methods*, 2024, DOI: 10.1039/D4AY01657B.



This is an Accepted Manuscript, which has been through the Royal Society of Chemistry peer review process and has been accepted for publication.

Accepted Manuscripts are published online shortly after acceptance, before technical editing, formatting and proof reading. Using this free service, authors can make their results available to the community, in citable form, before we publish the edited article. We will replace this Accepted Manuscript with the edited and formatted Advance Article as soon as it is available.

You can find more information about Accepted Manuscripts in the [Information for Authors](#).

Please note that technical editing may introduce minor changes to the text and/or graphics, which may alter content. The journal's standard [Terms & Conditions](#) and the [Ethical guidelines](#) still apply. In no event shall the Royal Society of Chemistry be held responsible for any errors or omissions in this Accepted Manuscript or any consequences arising from the use of any information it contains.

High Throughput Electronic Detection of Biomarkers Using Enzymatically Amplified Metallization on Nanostructured Surfaces

*Hanhao Zhang[‡], Neda Rafat[‡], Josiah Rudge, Sai Preetham Peddireddy, Yoo Na Kim, Taaseen Khan, Aniruddh Sarkar**

Georgia Institute of Technology, 315 Ferst Dr NW, Atlanta, GA 30332

KEYWORDS: Electrical Detection, Point-of-care Device, Nanoparticles, Diagnostics, COVID-19

* Corresponding author email address: aniruddh.sarkar@bme.gatech.edu

Analytical Methods Accepted Manuscript

1
2
3
4
5
6
7
8
9
10
11
12
13
14
15
16
17
18
19
20
21
22
23
24
25
26
27
28
29
30
31
32
33
34
35
36
37
38
39
40
41
42
43
44
45
46
47
48
49
50
51
52
53
54
55
56
57
58
59
60



1
2
3
4
5
6
7
8
9
10
11
12
13
14
15
16
17
18
19
20
21
22
23
24
25
26
27
28
29
30
31
32
33
34
35
36
37
38
39
40
41
42
43
44
45
46
47
48
49
50
51
52
53
54
55
56
57
58
59
60

ABSTRACT: Enzyme-linked immunosorbent assays are commonly used for clinical biomarker detection. However, they remain resource-intensive and difficult to scale globally. Here we present a miniaturized direct electronic biosensing modality which generates a simple and sensitive, quantitative, resistive readout of analyte binding in immunoassays. It utilizes the enhanced metallization generated by synergistic catalytic activity of nanostructured surfaces, created using gold nanoparticles, with enzymatic metallization, catalyzed by analyte-bound enzyme-labeled antibodies, to create a connected metal layer between microelectrodes. Based on this scheme, we develop a portable, high-throughput electronic biomarker detection device and platform which allows testing 96 different low volume (3 μ L) clinical samples in a handheld device. We find an analyte concentration-dependent tunable digital switch-like behavior in the measured resistance of this device. We use this system to further explore the mechanism of enhanced metallization and find optimal parameters. Finally, we use this platform to perform quantitative measurement of viral antigen-specific antibody titers from convalescent COVID-19 patient serum.

1. Introduction

The severe diagnostics shortage during the early stages of the COVID-19 pandemic underscored the inadequacy of current centralized laboratory-based diagnostics infrastructure in scaling rapidly to meet global needs during emerging infectious disease outbreaks¹. Arguably, lack of timely and easy-to-use diagnostics contributed to the failure of early public health efforts to contain the global spread of COVID-19. Sensitive and specific yet inexpensive and globally, rapidly scalable diagnostics modalities, especially those that are field-deployable and can be used at the point-of-care (POC), can help in early control of infectious disease outbreaks such as COVID-19, Ebola, MERS, H1N1 etc². Even now, as the global deployment of COVID-19 vaccines has occurred, scalable methods for sero-surveillance of biomarkers related to prior infection and vaccine efficacy are needed, especially due to the risk of emergence of vaccine-evading viral variants³. Multiplexed and high-throughput antibody-based biomarker measurements can enable this and these can be used as prognostic biomarkers as well ⁴.

Currently, enzyme-linked immunosorbent assays (ELISA) are the gold standard in quantitative detection of multiple categories of biomarkers ⁵. ELISAs provide high sensitivity (i.e. low limit of detection, LOD), specificity, repeatability and quantitative ability ⁶. However, they are based on sensitive optical measurement of enzymatic reaction products and require specialized instruments such as plate readers, which use optics, optical detectors (e.g. photomultiplier tubes) and automatic moving stages, all of which add to their high cost (usually >\$25,000) and size that restricts their usage to centralized laboratories by trained personnel. Efforts have been made to develop portable and/or inexpensive ELISAs ⁷, but a cost-versus-performance trade-off often exists due to the cost



1
2
3
4 of optical components, especially when miniaturized. This is exacerbated by the lower absorbance
5
6 path lengths as sample volumes are scaled down, requiring further higher optical detection
7
8 sensitivity in miniaturized versions ⁸. An inexpensive alternative is the lateral flow assay (LFA)
9
10 which often uses nano-conjugated antibodies (e.g. with gold nanoparticles) to return a output,
11
12 based on nanoparticle aggregation, that can be directly observed with the naked eye⁹. LFAs are
13
14 easy to use as well and are widely disseminated for POC diagnostics. However, LFAs are often
15
16 less sensitive and their result is binary (positive/negative)² which restricts their diagnostic value.


17
18 Electrical and electrochemical detection principles can be more suitable for POC diagnostics.
19
20 Instead of the use of intermediate optics, they convert immunobinding directly to an electronic
21
22 signal ¹⁰⁻¹⁷. Their size and cost can both be scaled down via miniaturization and integration using
23
24 microfabrication-based mass manufacturing¹⁰. These properties help them overcome
25
26 disadvantages of traditional ELISA including sample volume requirement and larger size/cost of
27
28 the required hardware^{18, 19}. Current electrochemical biosensors however often still remain too
29
30 complex to fabricate^{20, 21} or use especially in a high-throughput format, and are still rarely used in
31
32 the clinic ²².

33
34 Here, we set out to develop a miniaturize and broadly applicable direct electronic biosensing
35
36 modality that can exploit the sensitivity afforded by enzymatic amplification and yet generate a
37
38 simple, yet sensitive and quantitative electronic readout in an inexpensive portable platform. Gold
39
40 nanoparticle (AuNP) labeled probes are widely used in LFAs and silver reduction catalyzed by
41
42 them has been used for higher sensitivity in optical²³ and electronic^{24, 25} detection. We have recently
43
44 made a counter-intuitive observation that instead of using AuNP-labeled probes, immobilizing the
45
46
47
48
49
50
51
52
53
54
55
56
57
58
59
60

1
2
3 AuNPs on the chip surface creating a nanostructured catalytic surface provides >100X higher
4
5 sensitivity when coupled with enzymatic metallization²⁶. The mechanism underlying this enhanced
6
7 enzymatic metallization on AuNP-labeled nanostructured surfaces, however, remains unexplored.
8
9 Unlike the various works where AuNPs serve as the independent substrate for silver deposition to
10
11 occur on their surfaces^{27, 28}, here a combined effect from AuNPs, microscale interdigitated
12
13 electrodes (μ IDEs) and glass that form the nanostructure alters the amount of silver deposition.
14
15 Understanding it could hold the key to its optimization using various properties of AuNPs or other
16
17 nanomaterials and lead to higher sensitivity, ease-of-use and eventual clinical translation. Since it
18
19 is the combined effect of different parameters that determines the performance of the above
20
21 system, a high-throughput version of the above chip and corresponding hardware are necessary for
22
23 efficient screening. Additionally, such an easy-to-use portable chip and system would enable the
24
25 use of this method by others as well as help progress this detection modality towards clinical
26
27 applications.

28
29
30 In this work, we first developed a high-throughput micro-electrode array system for **ELISA** (or
31
32 EASyELISA) microchip to explore, optimize and clinically apply the above AuNP-driven
33
34 electronic immunoassay. This high-throughput EASyELISA microchip enables simultaneous
35
36 rapid testing of 96 different small volume (3 μ L) clinical samples, match the throughput of
37
38 conventional 96-well ELISA plates. We then used it to explore the combined effect of electrode
39
40 size, AuNP size and concentration on the performance of the microchip by running an
41
42 immunoassay for SARS-CoV-2 viral antigen-specific antibodies. We observed a tunable digital
43
44 switch-like behavior of the resistive readout versus antibody concentration where the switching
45
46
47
48
49
50
51
52
53
54
55
56
57
58
59
60

Open Access Article. Published on 05/11/2024. Downloaded on 05/11/2024 19:42:23. This article is licensed under a Creative Commons Attribution-NonCommercial 3.0 Unported Licence.



1
2
3 threshold was found to be tunable using electrode gap or AuNP size and concentration. Finally,
4
5 we developed a handheld cellphone-interfaced electronic reader for the EASyELISA microchip
6
7 which could automatically analyze 96 individual electrodes, thus building a full handheld plate
8
9 reader equivalent device and system. We then used the chip to measure quantitative electronic
10
11 readouts of SARS-CoV-2 Spike (S)-specific antibodies from convalescent COVID-19 patient
12
13 serum (n=5) and pre-pandemic healthy serum (n=3), performing serial dilution curves for titer
14
15 measurements, showing clear distinction between the two patient classes.
16
17

18 2. Materials and Methods

19 Soda lime glass wafers were purchased from UniversityWafer (Boston, MA). Phosphate buffer
20
21 saline (PBS) and Deionized (DI) water were purchased from Fisher Scientific (Hampton, NH).
22
23 Sodium Hydroxide, Poly-L-lysine solution, Bovine Serum Albumin (BSA), and gold nanoparticles
24
25 (AuNPs: 5nm/10nm/100nm) were purchased from Sigma Aldrich (St. Louis, MO). Tween 20 and
26
27 reagent alcohol were purchased from VWR (Radnor, PA). Polydimethylsiloxane (PDMS) sheet
28
29 was purchased from Greene Rubber Company (Woburn, MA). Pierce Bovine Serum Albumin,
30
31 Biotinylated, and HRP-Conjugated Streptavidin were purchased from ThermoFisher (Waltham,
32
33 MA). Enzymatic metallization substrate solution (EnzMet) was purchased from CedarLane
34
35 (Burlington, Canada). SARS-CoV-2 (2019-nCoV) spike recombinant protein was purchased from
36
37 Immune Technology (New York, NY). Recombinant Anti-SARS-CoV-2 Spike Glycoprotein S1
38
39 antibody was purchased from Abcam (Cambridge, United Kingdom). Mouse Anti-Human IgG Fc-
40
41 HRP was purchased from Southern Biotech (Birmingham, AL). Clinical serum samples
42
43 (healthy/SARS-Cov-2 patient) were purchased from RayBiotech (Peachtree Corners, GA). Vendor
44
45 obtained serum from donors with informed consent after IRB approval (PROTOCOL NO: SOP-
46
47 TF-PH-002 STERLING IRB ID: 8291-BZhang). Details are on file and available with the vendor.
48
49
50
51
52
53
54
55
56
57
58
59
60

Microfabrication of EASyELISA microchips

Soda Lime glass wafers were sonicated in acetone then isopropyl alcohol for 5 minutes each. Cleaned wafers were soaked in Piranha solution for 20 minutes. After rinsing with DI water (DIW) and drying, NR-9 1500PY Photoresist (Futurrex, Franklin, NJ) was spin coated and baked at 150°C for 2.5 minutes. Coated wafers then went through UV exposure (Karl Suss MA-6, Suss MicroTec, Germany), 1 minute baking at 100°C and development with RD-6 (Futurrex, Franklin, NJ). After 30 seconds of plasma descum (Vision 320 RIE, Plasma-therm, St. Petersburg, FL), 10 nm of titanium plus 100 nm of gold was deposited via e-beam evaporation (Denton Explorer, Denton Vacuum, Moorestown, NJ). Gold-coated wafers were then sonicated in acetone for 5 minutes to perform liftoff. After rinsing with isopropyl alcohol and drying, the wafers were diced (DAD3360, DISCO, Japan) to obtain individual chips.

Coating and preparation

Each diced chip was washed with 10% sodium hydroxide solution at 100 RPM for 2 hours then immersed in Poly-L Lysine solution for 30 minutes. After rinsing in DIW and drying, the chips were stored in a desiccator at room temperature under 40% humidity. PDMS sheet of 0.1mm thickness was laser-cut and washed in 5% Alconox in Deionized water (DIW). Before using the chip, the PDMS sheet was rinsed with DIW, cleaned by blotting with Scotch tape, then attached to the top of the chip to form the microwells around the electrodes.

Biotin-Streptavidin assay

Solution containing AuNPs of different sizes and concentrations were added to the wells and incubated in the wells for 45 minutes. Unless specified, all incubation was performed in a humidifier at room temperature (RT), followed by washing and drying. Washing procedure included placing the chip in a petri dish and washing with 0.1% Tween20 in PBS (PBST) at 60

1
2
3
4
5
6
7
8
9
10
11
12
13
14
15
16
17
18
19
20
21
22
23
24
25
26
27
28
29
30
31
32
33
34
35
36
37
38
39
40
41
42
43
44
45
46
47
48
49
50
51
52
53
54
55
56
57
58
59
60

Open Access Article. Published on 05/11/2024. Downloaded on 05/11/2024 19:42:21.
This article is licensed under a Creative Commons Attribution-NonCommercial 3.0 Unported Licence.



1
2
3 RPM for 5 minutes, then in PBS at 60 RPM for 5 minutes, then dipped in DIW. Washed chips were
4
5
6 dried with slide centrifuge (Labnet C1303-T) for 1 minute. Next, 1 mg/ml of biotin-BSA in PBS
7
8 was added to the wells and incubated for 1 hour. Without washing, the chip was blocked in 1%
9
10 BSA in PBST for 30 minutes. After washing and drying, 3.125 $\mu\text{g}/\text{ml}$ of HRP-SA was added and
11
12 incubated for 1 hour. Next, 1.6 μl of Enzmet A,B,C were subsequently added to the wells with
13
14 corresponding incubation time of 4, 4 and 7 minutes. The chips were then dipped in DI water,
15
16 dried with centrifuge and stored in petri dishes until resistance measurement.

17 18 19 **SARS-CoV-2 Antibody Assay**

20
21 Solution containing AuNPs of different sizes and concentrations were incubated in the wells for
22
23 45 minutes. 25 $\mu\text{g}/\text{ml}$ of SARS-Cov-2 Spike protein solution were added and incubated in the wells
24
25 overnight at 4°C. The chips were blocked as above. Different dilutions of anti-SARS-Cov-2 spike
26
27 human antibody were added to the wells and incubated for 1 hour. 1 $\mu\text{g}/\text{ml}$ of horseradish
28
29 peroxidase-conjugated anti-human IgG (anti-IgG-HRP) was then added and incubated for 30
30
31 minutes. Enzmet addition, drying and storage were performed as above. When running the assay
32
33 with clinical samples, the concentration of SARS-Cov-2 Spike protein was raised to 50 $\mu\text{g}/\text{ml}$ and
34
35 dilutions of patient/healthy samples in PBS were used instead of commercial antibody. All other
36
37 procedures remained the same.
38
39
40
41

42 43 **Assembly of the portable reader**

44
45 PmodIA impedance analyzer (Digilent), Analog multiplexer (ADG731, Analog Devices), Arduino
46
47 Nano, Bluetooth module (HC05, DSD Tech) and consumables (connector pins etc.) were
48
49 purchased from Digikey. Casings were printed with Form 2 (Formlabs) and F170 (Stratasys).
50
51

52 53 **Data Acquisition and Analysis**

1
2
3
4
5
6
7
8
9
10
11
12
13
14
15
16
17
18
19
20
21
22
23
24
25
26
27
28
29
30
31
32
33
34
35
36
37
38
39
40
41
42
43
44
45
46
47
48
49
50
51
52
53
54
55
56
57
58
59
60

Open Access Article. Published on 31 October 2024. Downloaded on 05/11/2024 19:42:21.
This article is licensed under a Creative Commons Attribution-NonCommercial 3.0 Unported Licence.



Optical images were taken via stereomicroscope (AmScope, CA), Scanning Electron Microscopy (SEM) images were taken via SU8010 SEM (Hitachi, Japan), and resistances were measured with a digital multimeter (Figure 1,3,5) or with the custom handheld reader. Data was analyzed with ImageJ and GraphPad Prism. All data presented are the arithmetic mean of at least 2 technical repeats and error bars represent standard deviation.

3. Results and Discussion

3.1 Demonstration of electronic detection using nanostructure surfaces

We first performed a model binding assay using biotinylated bovine serum albumin (biotin-BSA) as a capture agent and Horseradish Peroxidase labeled streptavidin (HRP-SA) as analyte. Microscale interdigitated electrodes (width and inter-electrode gap: 10 μ m) were made on glass wafers using standard microfabrication methods. The μ IDEs were coated with a poly-L-lysine (PLL) adhesive layer and stored in a desiccator. Before usage, a layer of laser-cut PDMS sheet was added on the top of the chip, forming microwells around the μ IDEs. For the group without AuNPs (Figure 1A), solution containing Biotin-BSA was directly added into the wells. HRP-SA and enzymatic metallization substrate were separately added following protocol in Methods section, resulting in silver deposition across the surface of μ IDEs. For the second group (Figure 1B), AuNPs (10nm, 1:50X diluted in DI water from an OD=1 stock, see supplementary Table 1) were first immobilized on the surface of μ IDEs. The stable immobilization via charge-based AuNP – lysine binding has been confirmed by various works^{29,30}. Biotin-BSA, HRP-SA and metallization substrate were subsequently added following the same protocol as the previous group. Significant

1
2
3 differences in deposited silver darkness were observed from the post-assay optical images (Figure
4 1C-E) of the μ IDEs. There was no silver deposited for the control group (no biotin-BSA or HRP-
5 SA) (Figure 1C). Small amount of silver was found for the μ IDE without AuNPs (Figure 1D).
6
7 However, a uniform dark layer of silver covered the entire μ IDE that had AuNPs pre-immobilized
8 (Figure 1E). This layer of silver acted as a conductor, connecting the gap between μ IDEs as a
9 bridge. With connected μ IDEs, a closed circuit would be formed when performing resistance
10 measurement. As detailed in previous work²⁶, such a decrease in resistance after the assay
11 suggested the presence of target molecules in the sample. A huge difference in resistance was
12 observed only for the group with HRP-SA and AuNP immobilization (Figure 1F). Scanning
13 electron microscopy (SEM) revealed further striking nanoscale differences. In the control μ IDE:
14 there were small silver deposits on the gold electrodes but none on the glass surface between
15 electrodes (Figure 1G). In the μ IDE with HRP-SA but without AuNPs: electrode surfaces were
16 found to have denser silver deposits but the glass surface between electrodes was found to have
17 sparse nanoparticulate silver deposits (~400nm) which had a characteristic ‘desert-rose’ shape, but
18 they were unconnected from each other (Figure 1H). This shape has been reported by others
19 previously^{31,32} as characteristic for enzyme-catalyzed
20
21
22
23
24
25
26
27
28
29
30
31
32
33
34
35
36
37
38
39
40
41
42
43
44
45
46
47
48
49
50
51
52
53
54
55
56
57
58
59
60

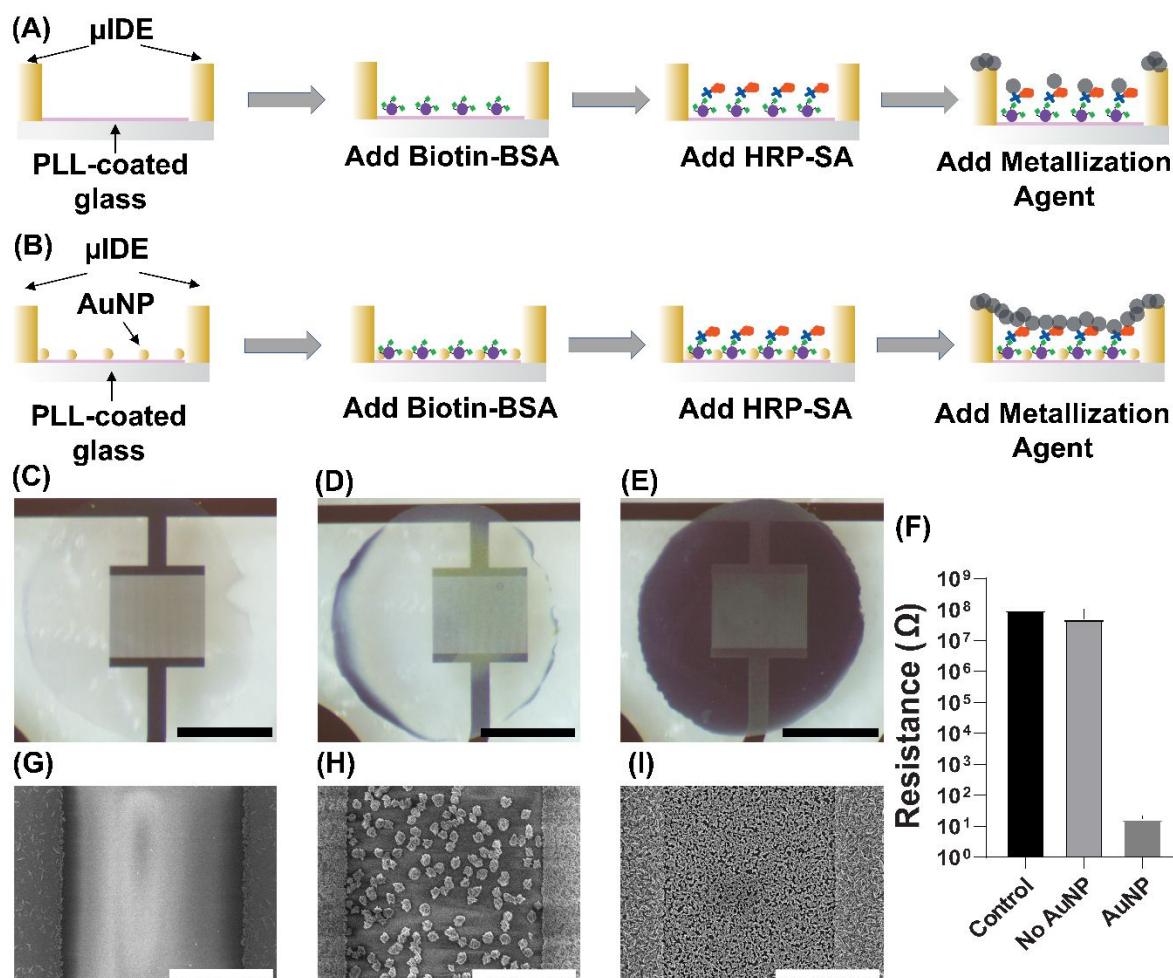


Figure 1. (A) Schematic of procedure of the model assay without using AuNP. (B) Schematic of procedure of the model assay with AuNP immobilized first. (C-E) Images of silver deposition on a μ IDE with no AuNP and no HRP (C), with HRP but no AuNP (D) and with both AuNP and HRP (E). Scale bars are 1000 μ m. (F) Resistance measured from the above three μ IDEs after silver deposition. (G) SEM images of the electrode in (C). (H) SEM image of the electrode in (D). (I) SEM image of the electrode in (E). Scale bars in the SEM images are 5 μ m.

silver nanoparticle formation. Finally, in the μ IDEs with HRP-SA and AuNP immobilization: while the electrode surfaces were found to have denser silver deposits here too, a starkly different

1
2
3 silver morphology was observed on the glass surface between electrodes, with a denser layer with
4
5 much larger number of smaller nano-particulates which merged to form a connected but perforated
6
7 mesh-like layer (Figure 1I). This change in silver morphology and density indicates a change in
8
9 deposition mechanism to a synergistic activity between enzymatic and AuNP-catalyzed silver
10
11 deposition.

12
13 We hypothesize that in absence of the AuNPs, the HRP molecules themselves nucleate
14
15 silver deposition sites which grow into unconnected larger nano-particulates (~400nm), while the
16
17 rest of the surface remains uncovered. This deposition is likely quenched by the eventual
18
19 inactivation of the enzymatic activity by silver deposition itself. However, with the nanostructured
20
21 catalytic surface resulting from AuNP immobilization, we hypothesize that the AuNPs act
22
23 preferentially as nucleation sites for the HRP-catalyzed metallization. Thus, a denser and
24
25 connected silver layer with smaller length-scale results which covers most of the surface. The
26
27 density and uniformity of silver are reflected by the resistance across μ IDEs. After enough silver
28
29 is deposited on the glass area between two electrodes, the silver acts as a conducting bridge,
30
31 forming a gold electrode-silver-gold electrode closed circuit. Measured resistance of the μ IDEs
32
33 showed an open circuit (10M Ω) for both the control μ IDE and the μ IDE with HRP-SA but without
34
35 AuNPs, whereas the resistance dropped to 100 Ω post-assay for the μ IDE with HRP-SA and
36
37 AuNPs. This establishes the dry-stable, simple resistive readout of this assay with six orders of
38
39 magnitude of change in resistance which enables its easy and inexpensive measurement in a fully
40
41 portable system.

42 3.2 Development of high-throughput electronic detection chip and portable reader system

43
44
45
46
47
48
49
50
51
52
53
54

We then fabricated the high-throughput EASyELISA chip with 96 μ IDE pairs (Figure 2A). This credit-card sized glass chip (76mm \times 55mm) had 12 rows \times 8 columns, with every pair of adjacent

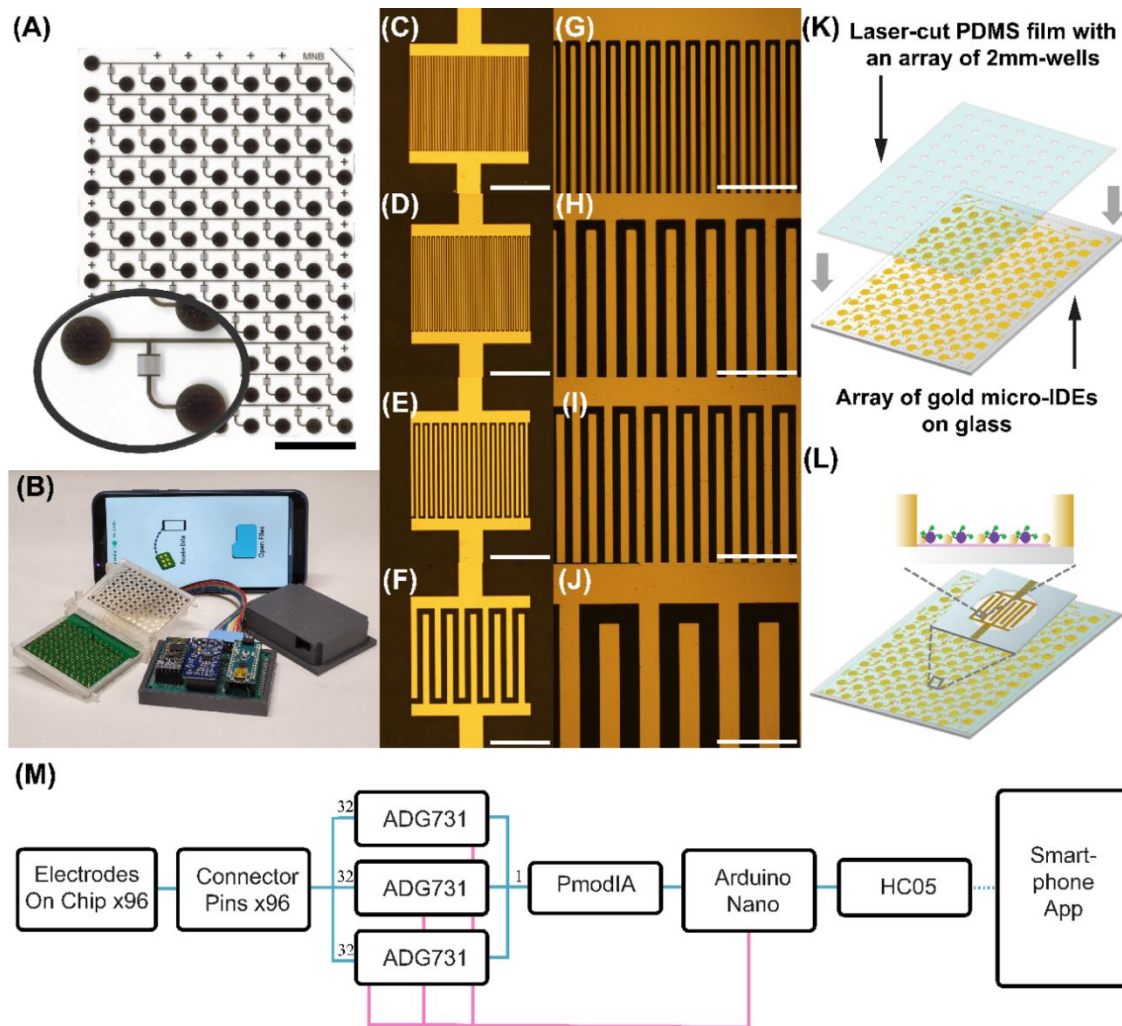


Figure 2. (A) Layout of microfabricated EASyELISA chip with zoomed in view of μ IDE and pads. Width and height of the chip are 26mm and 75mm. Scale bar is 15mm. Inset shows a zoomed-in image of a single μ IDE. (B) Portable reading system for the chip, including connector, analog front end, Bluetooth transmission module and an Android app on smartphone for hardware control and data visualization. (C-F) Brightfield images of the μ IDEs with 5 μ m,

 1
2
3
4
5
6
7
8
9
10
11
12
13
14
15
16
17
18
19
20
21
22
23
24
25
26
27
28
29
30
31
32
33
34
35
36
37
38
39
40
41
42
43
44
45
46
47
48
49
50
51
52
53
54
55
56
57
58
59
60

 Open Access Article. Published on 23 October 2024. Downloaded on 12/11/2024 12:42:21 PM.
This article is licensed under a Creative Commons Attribution-NonCommercial 3.0 Unported Licence.


1
2
3 10 μm , 20 μm and 50 μm gaps. Scale bars are 500 μm . (G-H) Zoomed in images of (C)-(F). Scale
4 bars are 80 μm for (G), (H) and 200 μm for (I), (J). (K) Assembly of PDMS layer on the chip. (L)
5 Schematic of the chip before loading sample with AuNP and capture molecule immobilized.
6
7 (M) Block diagram of the chip reader. Measurement signal pathways are shown as blue while
8 control signal pathways are shown as pink.

9
10
11
12
13
14
15
16
17
18
19
20
21
22
23
24
25
26
27
28
29
30
31
32
33
34
35
36
37
38
39
40
41
42
43
44
45
46
47
48
49
50
51
52
53
54
55
56
57
58
59
60

columns having μIDE pairs with the same electrode gaps and widths ($w = g = 5\mu\text{m}$, 10 μm , 20 μm
and 50 μm , Figure 2C-J). Additionally, the inter-column gap made the chip compatible with
standard multi-channel pipettes for high-throughput assays. This chip was then visually aligned
and assembled, via reversible bonding, with a thin (0.01") laser-cut PDMS microwell array (Figure
2K) which enables loading of small volumes (~1.5-3 μL) of samples and reagents reliably in a high-
throughput yet leak-free manner. This enables performing 96 different assays on the individual
 μIDEs (Figure 2L) on a single chip. Compared to conventional ELISA, here a 10-80-fold reduction
of the sample volume to only 3 μL each is achieved. Also, washing and drying of the chip can be
done by placing the entire chip in wash buffer and micro-centrifuging or blow drying respectively.
This saves the effort of additional pipetting and draining steps or the need for any pumps or tubing
needed for traditional microfluidic chips and is more akin to standard slide-based assays^{33, 34}.
Additionally, to enable ease of rapid electronic measurement in a POC-compatible manner, an
inexpensive handheld measurement system was built (Figure 2B). A custom printed circuit board
was designed with 96 spring-mounted pogo-pins and assembled inside a 3D-printed enclosed
connector which enabled easy connection to all 96 μIDEs . As shown in the block diagram (Figure

1
2
3
4
5
6
7
8
9
10
11
12
13
14
15
16
17
18
19
20
21
22
23
24
25
26
27
28
29
30
31
32
33
34
35
36
37
38
39
40
41
42
43
44
45
46
47
48
49
50
51
52
53
54
55
56
57
58
59
60

2M), signal from the connectors was routed via three 32-plex analog multiplexers (ADG731) which allow the digital selection of a single μ IDE for measurement by an Arduino Nano. The selected output is then connected to a PmodIA Impedance analyzer module. This module has an AD5933 12-bit impedance converter chip with a frequency generator which excited the device under test and an analog-to-digital converter to capture the response. A discrete Fourier transform is performed automatically on chip and the real and imaginary parts of the response can be relayed via serial communication, to an Arduino Nano and sent to a smartphone via a Bluetooth module. A custom Android application was developed which not only controlled the above operations but also visualized the received data and enabled its cloud-based storage. Details of the design of the chip, system and application can be found via links in supplementary information. By measuring resistance value for eight different resistors ranging from 100 ohms to 210000 ohms with both the reader and the multimeter, we found a high correlation of $r = 0.999958$ between the two methods (Fig S1), proving equivalence of the two in our application. We note that this reader hardware itself is effectively a portable 96-channel impedance analyzer or LCR meter which can be useful beyond its application with the EASyELISA chip here as well.

3.3 Optimization of electronic immunoassay on high-throughput electronic detection chip

We then applied the EASyELISA chip to a SARS-CoV-2 viral antigen-specific antibody detection assay, with an anti-Spike monoclonal antibody (anti-S mAb) as the target and performed a parametric study and optimization (Figure 3A). To study the interaction between the AuNPs, μ IDEs and the enzymatic metallization (quantified by measured resistance readout), we selected inter-electrode gap, g (while maintaining $w = g$), concentration and size of AuNPs as the three

target parameters. First, the effect of varying g was explored with AuNPs of a particular size and concentration (10nm, 1:10X diluted). AuNPs and S antigen were immobilized on the chip as above, followed by incubation with serial dilutions of anti-S mAbs and then with HRP-labeled anti-human IgG probe followed by the metallization. As shown in Figure 3B, four groups of 6-point serial sample dilution curves with two replicates each were generated on a single chip. Within the first six electrodes in each group, the concentration of sample decreased from left to right. A systematic variation in the darkness of the deposited silver in the microwells, correlated with the sample dilutions, was observed. Resistance measurement results from this experiment are shown in Figure 3C. μ IDE resistances are found to reduce systematically with increasing anti-S mAb concentration. Resistance versus concentration curves are observed to form the typical sigmoidal shape seen in traditional ELISAs. The top of the curve ($>50M\Omega$) corresponds to low anti-S mAb concentrations and the bottom ($10k\Omega$) corresponds to high concentrations of anti-S mAb. This establishes the operation of the high-throughput EASyELISA chip and assay with a direct resistive electronic readout.

Notably, here, the large (>5000 -fold) resistance change observed occurs over ~ 5 - 10 -fold change in anti-S mAb concentration. This can be contrasted with the 25 - 100 -fold change in analyte concentration over which typical ELISA optical signal vs concentration sigmoidal curves run from top to bottom⁵. Thus, EASyELISA is found to have a sharper transition and switch-like characteristic compared to traditional ELISAs. The switching point is defined as the point where the slope of resistance increases dramatically. Physically, it is the concentration of sample whose corresponding silver changes from a uniform dense layer to a sparse layer. The silver particles are

no longer closely attached to each other, making electrons harder to travel between gold electrodes when a voltage is applied. This loose connection of silver particle results in resistance increasing dramatically. This could indicate a potential cooperativity-like mechanism underlying the silver deposition. Additionally, it also relates back to the nanoscale morphology of the deposited silver which grows as separate particles and then merges rather than just growing thicker as a continuous layer.

Five parameter asymmetric logistic curves were fitted to the data and the extracted EC50 values, which represent a metric for the switching points, were found to systematically increase with the electrode gap (Figure 3C). We infer from this that the connectivity of the nanoscale mesh-like silver layer (Figure 1I), may have a characteristic microscale length-scale as well which grows with analyte concentration and once it increases above the electrode gap size, closed electrode is observed. Thus, μ IDEs with lower gap switch at lower analyte concentrations. Overall, smaller inter-electrode gap sizes thus provide better sensitivity or lower LODs. Beyond the switching point, at a given anti-S mAb concentration, resistances for μ IDEs were found to vary with the electrode gap ($\propto \frac{1}{g^{1.5}}$). Theoretically, a $\frac{1}{g^2}$ dependence is expected due to the increase in number of electrodes in a given area. This indicates that there may be other secondary effects involved such as the effect of electrode gap on silver deposition.

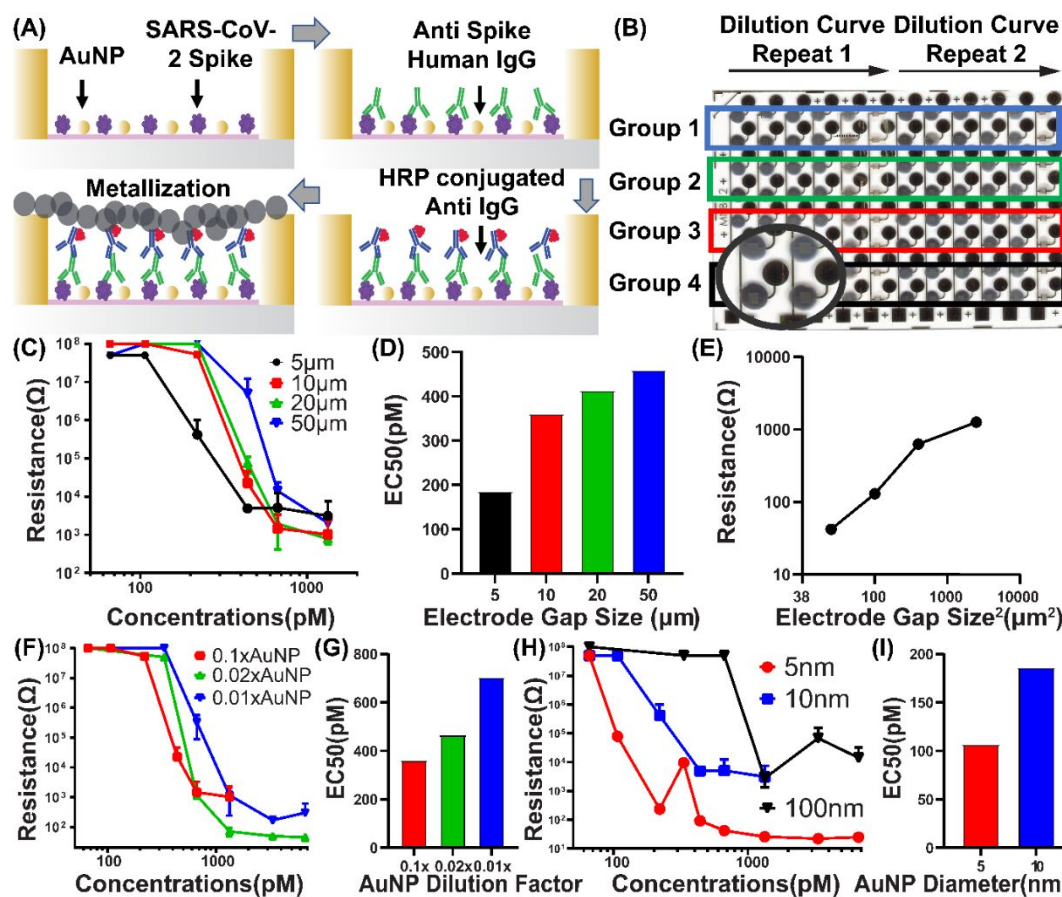


Figure 3. (A) Schematic of assay workflow. (B) Optical image of the chip after metallization. μ IDEs with four different gaps are fabricated on the same chip, indicated here as: black: 5 μ m, red: 10 μ m, green: 20 μ m, blue: 50 μ m. Inset shows zoomed-in view of μ IDEs. (C, D) Resistance reading and EC₅₀ from dilution curves of anti-S mAb using 1:10X 10nm AuNP across different electrode gaps. (E) Resistance versus square of electrode gap at 1.33nM of anti-S mAb. (F, G) Resistance reading and EC₅₀ from dilution curves of anti-S mAb using 10nm AuNP on 5 μ m electrode gaps across different AuNP concentrations. (H, I) Resistance reading and EC₅₀ from dilution curves of SARS-Cov-2 spike antibody using 0.1x AuNP on 5 μ m electrode gaps with

1
2
3 different AuNP diameters. Each group has a repeat number $n = 2$, standard deviations are shown
4
5 as error bars.

6
7
8
9 Finally, we compared the effect of AuNP size by running the serial anti-S mAb dilutions with 5nm,
10
11 10nm and 100nm AuNPs (at 1:10X dilution) on $g = 5\mu\text{m}$ electrodes. All the assays showed switch-
12
13 like characteristics (Figure 3H). The switching point was found to shift to lower sample
14
15 concentrations as the AuNP size was reduced (Figure 3I). However, unlike with the earlier
16
17 parameters, here, we see AuNP sizes also drive much larger differences in resistance e.g. entire
18
19 impedance curve of 5nm AuNPs (red) is below that of the 10nm AuNPs (blue). On the other hand,
20
21 the 100nm AuNPs do not drive the μIDE resistance to a fully closed low impedance state, whose
22
23 resistance reached hundred-million ohms range when the concentration was still around nano
24
25 molar. Similar trends were seen with μIDEs with $g = 10\mu\text{m}$ (Figure S3). Overall, this is indicative
26
27 of lower AuNP sizes driving significantly higher silver deposition in a sample and thus enzyme
28
29 concentration-dependent manner. This could be due to higher AuNP counts or higher effective
30
31 areas or area-to-volume ratios of the smaller AuNPs contributing to the higher synergistic catalytic
32
33 activity of the nanostructured surface generated by them. Earlier work on catalytic properties of
34
35 AuNPs has also observed similar trends with size³⁵. Here, this indicates that 5nm AuNPs will
36
37 provide the highest sensitivity. The EC50 of the S mAb serial dilution curve with 5nm AuNPs was
38
39 ~100pM indicating a 10-100pM scale LOD.

40
41
42
43
44
45
46
47
48
49
50
51 Next, given the complex variation of LOD with AuNP parameters observed above, we investigated
52
53 how AuNPs affect silver deposition by performing SEM imaging on them (Figure 4a-d) and their
54
55 corresponding silver metallization (Figure 4E-H). We analyzed the immobilized AuNP count,
56
57
58
59
60

surface area and average inter-particle gap of each of the AuNP conditions from SEM images and studied the variation of the assay LOD with these parameters. Results showed that the AuNP count

Analytical Methods Accepted Manuscript

1
2
3
4
5
6
7
8
9
10
11
12
13
14
15
16
17
18
19
20
21
22
23
24
25
26
27
28
29
30
31
32
33
34
35
36
37
38
39
40
41
42
43
44
45
46
47
48
49
50
51
52
53
54
55
56
57
58
59
60

Open Access Article. Published on 20 April 2024. Downloaded on 05/11/2024 19:42:23.
This article is licensed under a Creative Commons Attribution-NonCommercial 3.0 Unported Licence.



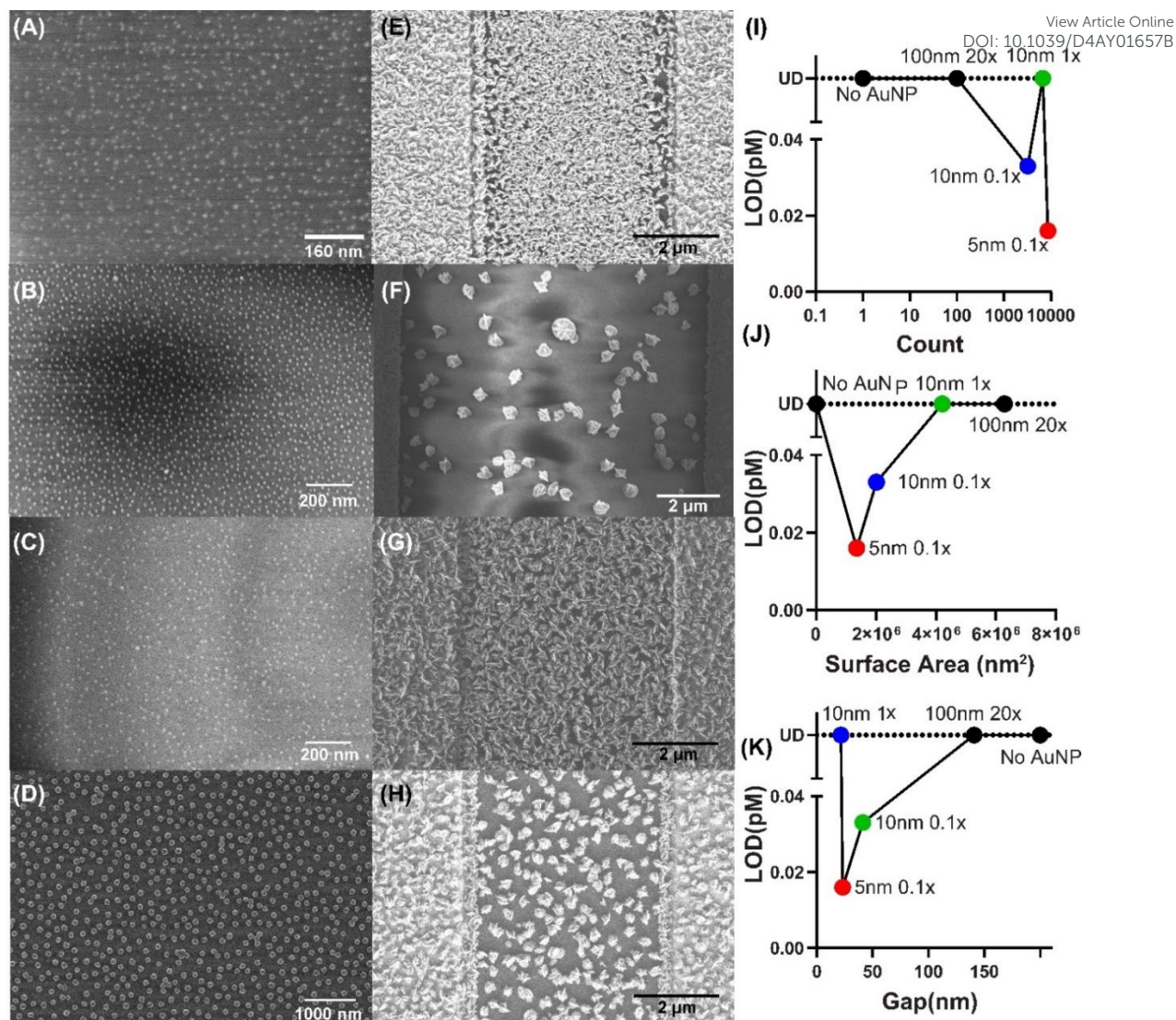


Figure 4. SEM images, before adding capture antigen, of (A) 0.1X 5nm AuNP (B) 1X 10nm AuNP (C) 0.1X 10nm AuNP (D) 20X 100nm AuNP. SEM images of silver metallization, after immunoassay, using (E) 0.1x 5nm AuNP (F) 1X 10nm AuNP (G) 0.1X 10nm AuNP (H) 20X 100nm AuNP. (I) Limit of detection vs different AuNP counts. (J) Limit of detection vs different AuNP surface areas. (K) Limit of detection vs different AuNP inter-particle gaps.

or surface area occupied by AuNPs alone does not determine the amount of silver deposition and LOD (Figure 4I, J).

1
2
3
4
5
6
7
8
9
10
11
12
13
14
15
16
17
18
19
20
21
22
23
24
25
26
27
28
29
30
31
32
33
34
35
36
37
38
39
40
41
42
43
44
45
46
47
48
49
50
51
52
53
54
55
56
57
58
59
60

Finally, we studied the effect of inter-AuNP gap size (Figure 4K) and observed that there may be an optimal inter-particle gap which results in the lowest (i.e. best) LOD.

We hypothesize that enzymatic silver metallization at the AuNPs as nucleation sites, then grows around these seeds which then merge and form the connected mesh eventually. Thus, AuNPs further apart result in higher analyte LODs as higher enzyme concentrations are needed to fill the higher inter-particle gaps. On the other hand, the S protein, used as capture antigen here, is reported to be ~21nm in length³⁶⁻³⁸. Thus, it is plausible that too small an inter-particle gap blocks the capture antigen binding. Overall, we conclude that a dense layer of small AuNPs with gap size slightly larger than 20nm provides the highest enzymatic silver metallization and best LOD.

View Article Online
DOI: 10.1039/C4AY01657B

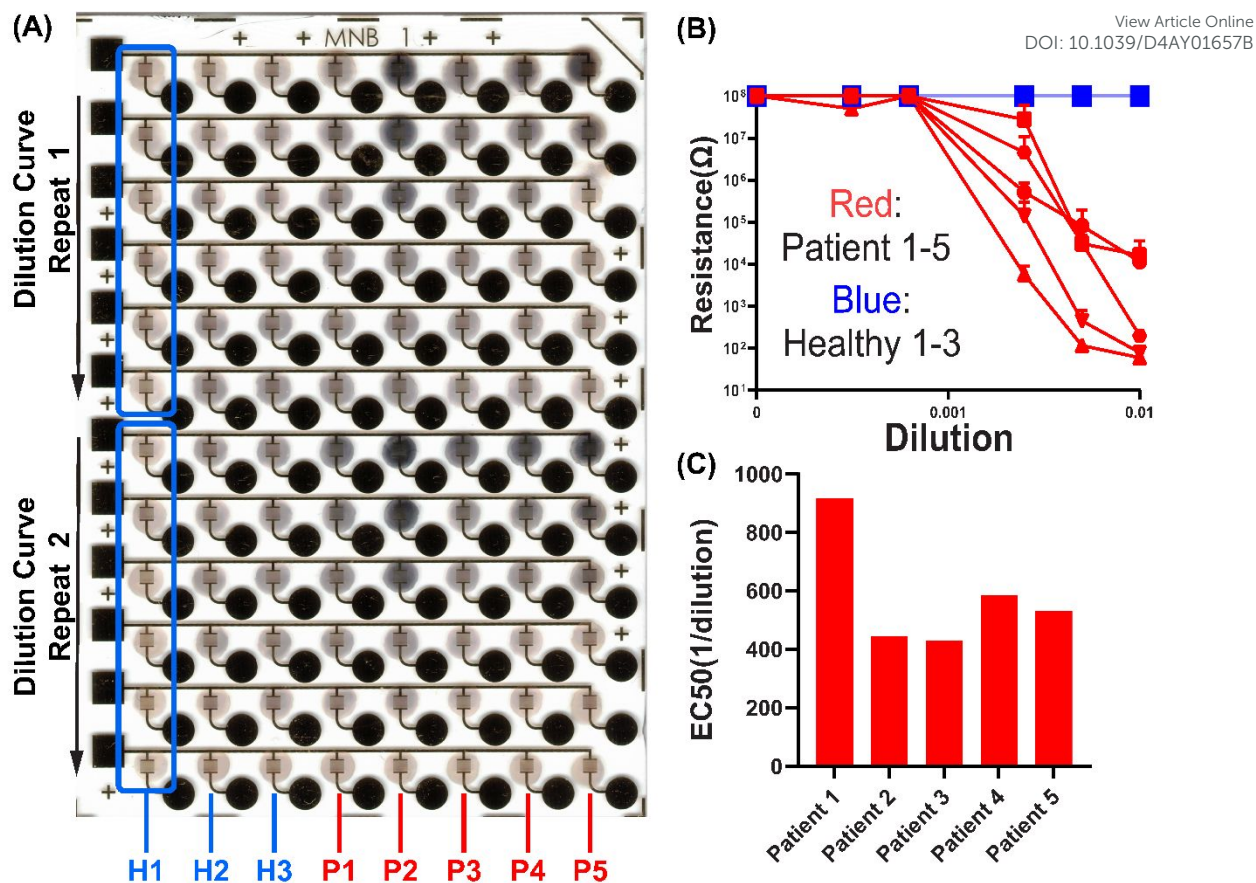


Figure 5. (A) Optical image of the chip after running the assay with healthy and SARS-CoV-2 samples. Each column corresponds to an individual sample. Within each column (example: boxed section for H1), a dilution curve is performed on Row 1-5 with decreasing concentration while Row 6 is the PBS control. Row 7-12 are repeats of Row 1-6. (B) Resistance readings of the patient and healthy samples. (C) EC₅₀ of the five patient samples. All healthy samples form open circuit and EC₅₀ cannot be derived. Each group has a repeat number $n = 2$, standard deviations are shown as error bars.

3.4 Clinical immunoassay for electronic detection of viral antigen-specific antibodies

Given the above results, we selected 1:10X 5nm AuNPs on μ IDEs with 5 μ m gaps to perform a clinical immunoassay. Dilution curves of 5 convalescent COVID-19 patient serum samples and



3 pre-pandemic healthy serum, with two technical repeats, were run on a single chip (Figure 5). Clear differences in silver metallization were observed between patient and healthy samples (Figure 5A). Resistance readings for all healthy samples were all around $100M\Omega$ at all dilutions while lower dilution-dependent resistances were obtained from all patient samples (Figure 5B). Fitted EC50s are obtained as anti-S antibody titers for the patient serum samples (Figure 5C). This shows that the EASyELISA microchip developed here can be used for clinical immunoassays with quantitative readout of titers of antibody-based biomarkers.

4. Conclusion

Here we presented a miniaturized electronic biosensing modality which generates a simple yet sensitive resistive readout. It utilizes the enhanced metallization generated by the synergistic catalytic activity of a nanostructured surface created using AuNPs with enzymatic metallization. We developed a high-throughput microchip which allows testing 96 different low volume ($3\mu\text{L}$) clinical samples with the ease-of-use afforded by multichannel pipette compatibility and a handheld cellphone-interfaced reader, which enabled the below advantages: compared to conventional 96-well ELISA, it requires less sample volume and smaller/cheaper portable hardware; compared to lateral flow assay, it enables quantitative instead of binary result. Compared to field-effect transistor-based electrochemical biosensors^{20, 21, 39} (Table S1), it is easier to fabricate and enables dry measurement/storage and re-measurement. Due to its unique metallization-based sensing mechanism, the major advantages include repeatability and signal degradation due to oxidation if the chip is not handled properly. Using this chip, we found a tunable digital switch-like response characteristic in antibody detection, where the switching threshold is tunable using various AuNP and device parameters. We also explored the mechanism of synergistic enhancement of metallization and optimized it

1
2
3
4
5
6
7
8
9
10
11
12
13
14
15
16
17
18
19
20
21
22
23
24
25
26
27
28
29
30
31
32
33
34
35
36
37
38
39
40
41
42
43
44
45
46
47
48
49
50
51
52
53
54
55
56
57
58
59
60

Downloaded on 05/12/24 19:42:33
This article is licensed under a Creative Commons Attribution-NonCommercial 3.0 Unported Licence.



via high-throughput parametric variation. We found that small electrode gaps and AuNP sizes enhance the assay sensitivity. Higher AuNP density, or lower inter-AuNP gaps, also enhanced sensitivity up to a certain optimum. Overall, we find evidence supporting a proposed mechanism that enzyme-catalyzed metallization is nucleated on AuNPs on the surface and grows to merge as an electrically connected mesh-like layer. Further work is needed to establish this mechanism via generalizing to other nanomaterials (e.g. nanowires) and capture molecules. Finally, using this platform we also demonstrate the detection and quantitation of antiviral antigen-specific antibodies from convalescent COVID-19 patient serum. The silver deposited on the chip is dry-stable, which provides a way to preserve the result of a clinical immunoassay directly on the chip as well. However, one current limitation of this is, due to oxidation of the deposited metal on the electrode, the resistance readings from the chip can drift in the long term (~days) unless stored in air-tight containers with inert gas, limiting the stability of the result in case repeated measurement is needed. However, ELISA suffers from the same drawback as the liquid inside the well could evaporate, modifying the amount of absorbance unless properly sealed and stored. Further future work would include applying this platform to other binding-based assays of clinical utility (including DNA, RNA, cells, etc.) and test the specificity if required by application, thus developing a versatile POC-compatible electronic biosensing system.

Resource availability


Corresponding contact

Further information and requests for resources and reagents should be directed to and will be fulfilled by the corresponding contact:

Aniruddh Sarkar (aniruddh.sarkar@bme.gatech.edu).

1
2
3
4
5
6
7
8
9
10
11
12
13
14
15
16
17
18
19
20
21
22
23
24
25
26
27
28
29
30
31
32
33
34
35
36
37
38
39
40
41
42
43
44
45
46
47
48
49
50
51
52
53
54
55
56
57
58
59
60

Downloaded on 05/12/2024 19:42:33
This article is licensed under a Creative Commons Attribution-NonCommercial 3.0 Unported Licence.



All the code and AutoCAD designs of the chips can be accessed using the Github links in Supplementary file. All data reported used in this work will be shared by the corresponding authors on request.

Supplemental information

Links to Github for hardware design files/code. Comparison between current work and existing works on detection assays utilizing enzyme, metal deposition and gold. (Table S1) Properties of AuNP stock solutions (Table S2); Correlation between resistance reading obtained from the portable reader and that of a digital multimeter (Figure S1); Resistance of μ IDE using 1X 10nm AuNP on 5 μ m electrodes (Figure S2); Resistance of μ IDE using different AuNP sizes on 10 μ m electrode gap (Figure S3); AuNP image analysis (Figure S4). Procedure of microfabricating the EASyELISA chip (Figure S5); Close-up views of the portable reader (Figure S6).

Acknowledgement

Microfabrication of chips was done with support from staff and facilities of the Institute for Electronics and Nanotechnology (IEN) at Georgia Tech.

Author Contributions

H. Zhang: conceptualization, methodology, investigation, validation, data curation, formal analysis, visualization, software, writing – original draft, writing – review & editing. N. Rafat: conceptualization, methodology, investigation, validation, formal analysis, writing – review & editing. J. Rudge: investigation, validation, data curation, formal analysis, software, writing – review & editing. S. Peddireddy: investigation, formal analysis, writing – review &

editing. Y. Kim: software, formal analysis, writing – review & editing. T. Khan: View Article Online
DOI: 10.1039/D4AY01657B

investigation, writing – review & editing. A. Sarkar: conceptualization, methodology, formal analysis, writing – review & editing resources, supervision, project administration, funding acquisition. All authors reviewed the manuscript.

Funding Sources

This work was funded by the National Institute of Health (NIH, R01AI182322).

Notes

H. Z, N.R. and A.S. are co-inventors of a patent application related to the nanoparticle-enhancement method for electronic biomarker detection.

References

1. O. Vandenberg, D. Martiny, O. Rochas, A. van Belkum and Z. Kozlakidis, *Nature Reviews Microbiology*, 2021, **19**, 171-183.
2. Y. Zhou, Y. Wu, L. Ding, X. Huang and Y. Xiong, *TrAC Trends in Analytical Chemistry*, 2021, **145**, 116452.
3. C. f. D. C. a. Prevention, COVID-19 Serology Surveillance Strategy, <https://www.cdc.gov/coronavirus/2019-ncov/covid-data/serology-surveillance/index.html>, (accessed Apr. 12, 2023).
4. S. P. Peddireddy, S. A. Rahman, A. R. Cillo, G. M. Vijay, A. Somasundaram, C. J. Workman, W. Bain, B. J. McVerry, B. Methe, J. S. Lee, P. Ray, A. Ray, T. C. Bruno, D. A. A. Vignali, G. D. Kitsios, A. Morris, H. Singh, A. Sarkar and J. Das, *Cell Reports*, 2022, **39**.
5. J. R. Crowther, *Methods Mol Biol*, 2000, **149**, Iii-iv, 1-413.
6. S. Hosseini, P. Vázquez-Villegas, M. Rito-Palomares and S. O. Martinez-Chapa, in *Enzyme-linked Immunosorbent Assay (ELISA): From A to Z*, eds. S. Hosseini, P. Vázquez-Villegas, M. Rito-Palomares and S. O. Martinez-Chapa, Springer Singapore, Singapore, 2018, DOI: 10.1007/978-981-10-6766-2_5, pp. 67-115.
7. A. Zhdanov, J. Keefe, L. Franco-Waite, K. R. Konnaiyan and A. Pyayt, *Biosensors and Bioelectronics*, 2018, **103**, 138-142.
8. K. Grabowska, X. Wang, A. Jacobsson and J. Dillner, *J Immunol Methods*, 2002, **271**, 1-15.
9. B. G. Andryukov, *AIMS Microbiol*, 2020, **6**, 280-304.
10. K. Kikkeri, D. Wu and J. Voldman, *Lab Chip*, 2021, **22**, 100-107.

- 1
2
3
4
5
6
7
8
9
10
11
12
13
14
15
16
17
18
19
20
21
22
23
24
25
26
27
28
29
30
31
32
33
34
11. S. S. Mahshid, S. E. Flynn and S. Mahshid, *Biosensors and Bioelectronics*, 2021, **176**, 112905. View Article Online
DOI: 10.1039/D1AY01657B
12. J. Mok, M. N. Mindrinos, R. W. Davis and M. Javanmard, *Proc Natl Acad Sci U S A*, 2014, **111**, 2110-2115.
13. J. Rudge, M. Hoyle, N. Rafat, A. Spitale, M. Honan and A. Sarkar, *ACS Omega*, 2023, DOI: 10.1021/acsomega.3c01939.
14. M. Seifert, E. Vargas, V. Ruiz-Valdepenas Montiel, J. Wang, T. C. Rodwell and A. Catanzaro, *Sci Rep*, 2021, **11**, 19193.
15. R. Zeng, M. Qiu, Q. Wan, Z. Huang, X. Liu, D. Tang and D. Knopp, *Analytical Chemistry*, 2022, **94**, 15155-15161.
16. Z. Yu, H. Gong, J. Xu, Y. Li, Y. Zeng, X. Liu and D. Tang, *Analytical Chemistry*, 2022, **94**, 3418-3426.
17. X. Wang, H. Wang, X. Wan, Q. Wei, Y. Zeng and D. Tang, *Biosensors and Bioelectronics*, 2025, **267**, 116749.
18. S. Lv, K. Zhang, L. Zhu, D. Tang, R. Niessner and D. Knopp, *Analytical Chemistry*, 2019, **91**, 12055-12062.
19. Y. Wang, R. Zeng, S. Tian, S. Chen, Z. Bi, D. Tang and D. Knopp, *Analytical Chemistry*, 2024, **96**, 13663-13671.
20. D. S. Juang, C.-H. Lin, Y.-R. Huo, C.-Y. Tang, C.-R. Cheng, H.-S. Wu, S.-F. Huang, A. Kalnitsky and C.-C. Lin, *Biosensors and Bioelectronics*, 2018, **117**, 175-182.
21. C. K. Tang, A. Vaze, M. Shen and J. F. Rusling, *ACS Sensors*, 2016, **1**, 1036-1043.
22. C. D. Chin, V. Linder and S. K. Sia, *Lab Chip*, 2012, **12**, 2118-2134.
23. T. Laksanasopin, T. W. Guo, S. Nayak, A. A. Sridhara, S. Xie, O. O. Olowookere, P. Cadinu, F. Meng, N. H. Chee, J. Kim, C. D. Chin, E. Munyazesa, P. Mugwaneza, A. J. Rai, V. Mugisha, A. R. Castro, D. Steinmiller, V. Linder, J. E. Justman, S. Nsanzimana and S. K. Sia, *Sci Transl Med*, 2015, **7**, 273re271.
24. Y. Liu, D. Zhang, E. C. Alocilja and S. Chakrabarty, *Nanoscale Res Lett*, 2010, **5**, 533-538.
25. S. J. Park, T. A. Taton and C. A. Mirkin, *Science*, 2002, **295**, 1503-1506.
26. N. Rafat, H. Zhang, J. Rudge, Y. N. Kim, S. P. Peddireddy, N. Das and A. Sarkar, *Small*, 2022, **18**, 2203309.
27. H. Liu, B. Liu, P. Huang, Y. Wu, F. Y. Wu and L. Ma, *Mikrochim Acta*, 2020, **187**, 551.
28. J. Chen, A. A. Jackson, V. M. Rotello and S. R. Nugen, *Small*, 2016, **12**, 2469-2475.
29. N. P. Goode, M. Shires and A. M. Davison, *Histochemistry*, 1992, **98**, 67-72.
30. K. Rahme, G. Minassian, E. Ghanem, M. Nakhil, R. El Hage, E. Souaid and J. D. Holmes, 2018.
31. T. Schüler, A. Steinbrück, G. Festag, R. Möller and W. Fritzsche, *Journal of Nanoparticle Research*, 2009, **11**, 939-946.
32. H. Schneidewind, T. Schüler, K. K. Strelau, K. Weber, D. Cialla, M. Diegel, R. Mattheis, A. Berger, R. Möller and J. Popp, *Beilstein Journal of Nanotechnology*, 2012, **3**, 404-414.
33. N. Rafat, L. Brewer, N. Das, D. J. Trivedi, B. K. Kaszala and A. Sarkar, *ACS Sens*, 2023, DOI: 10.1021/acssensors.2c01429.
34. G. Zhou, S. Bergeron and D. Juncker, *J. Proteome Res.*, 2015, **14**, 1872-1879.

- 1
2
3
4
5
6
7
8
9
10
11
12
13
14
15
16
17
18
19
20
21
22
23
24
25
26
27
28
29
30
31
32
33
34
35
36
37
38
39
35. B. Hvolbæk, T. V. W. Janssens, B. S. Clausen, H. Falsig, C. H. Christensen and J. K. Nørskov, *Nano Today*, 2007, **2**, 14-18.
36. L. Tai, G. Zhu, M. Yang, L. Cao, X. Xing, G. Yin, C. Chan, C. Qin, Z. Rao, X. Wang, F. Sun and Y. Zhu, *Proceedings of the National Academy of Sciences*, 2021, **118**, e2112703118.
37. Y. Cai, J. Zhang, T. Xiao, H. Peng, S. M. Sterling, R. M. Walsh, S. Rawson, S. Rits-Volloch and B. Chen, *Science*, 2020, **369**, 1586-1592.
38. B. Turoňová, M. Sikora, C. Schürmann, W. J. H. Hagen, S. Welsch, F. E. C. Blanc, S. von Bülow, M. Gecht, K. Bagola, C. Hörner, G. van Zandbergen, J. Landry, N. T. D. de Azevedo, S. Mosalaganti, A. Schwarz, R. Covino, M. D. Mühlebach, G. Hummer, J. Krijnse Locker and M. Beck, *Science*, 2020, **370**, 203-208.
39. A. C. Glavan, D. C. Christodouleas, B. Mosadegh, H. D. Yu, B. S. Smith, J. Lessing, M. T. Fernández-Abedul and G. M. Whitesides, *Analytical Chemistry*, 2014, **86**, 11999-12007.

View Article Online
DOI: 10.1039/D4AY01657B



The data supporting this article have been included as part of the Supplementary Information.

Analytical Methods Accepted Manuscript

1
2
3
4
5
6
7
8
9
10
11
12
13
14
15
16
17
18
19
20
21
22
23
24
25
26
27
28
29
30
31
32
33
34
35
36
37
38
39
40
41
42
43
44
45
46
47
48
49
50
51
52
53
54
55
56
57
58
59
60

Open Access Article. Published on 20 April 2024. Downloaded on 05/11/2024 19:42:23.
This article is licensed under a Creative Commons Attribution-NonCommercial 3.0 Unported Licence.

